Electron Spin Transport in a Metal-Oxide-Semiconductor Si Two-Dimensional Inversion Channel: Effect of Hydrogen Annealing on Spin-Scattering Mechanism and Spin Lifetime

Shoichi Sato,[1,2,*] Masaaki Tanaka,[1,2,†] and Ryosho Nakane[1,‡]

[1] *Department of Electrical Engineering and Information Systems, The University of Tokyo, 7-3-1 Hongo, Bunkyo-ku, Tokyo 113-8656, Japan*

[2] *Center for Spintronics Research Network (CSRN), The University of Tokyo, 7-3-1 Hongo, Bunkyo-ku, Tokyo 113-8656, Japan*

(Received 31 March 2022; revised 31 October 2022; accepted 1 November 2022; published 23 December 2022)

Electron spin transport in a two-dimensional Si inversion channel is experimentally and theoretically studied in terms of electron distribution in the subbands, electron momentum scattering processes, electron momentum lifetime, and spin lifetime. The electrical properties, electron charge transport, and spin transport are investigated by measuring a Si-based spin metal-oxide-semiconductor field-effect transistor with a 10-μm channel length under various bias and temperature conditions (4, 77, 150, and 295 K). In particular, in our unique procedure, the same device is measured before and after annealing to quantitatively clarify the change in the spin transport with lower and higher electron mobilities, by excluding device-to-device variability. Even when the distribution of electrons in the subbands, electron mobility, and temperature are significantly changed, the spin-flip probability, which is defined as the ratio of electron momentum lifetime to spin lifetime, is nearly constant at approximately 1/25 000, probably due to the Elliot-Yafet mechanism. The estimated spin conservation lengths at various temperatures are increased 2–50 times with increases in both the electron mobility and spin drift. With a high electron mobility of 3065 $\mathrm{cm^2V^{-1}s^{-1}}$ at 4 K, spin transport with a spin conservation efficiency of 94% is achieved through the 10-μm-long channel.

DOI: 10.1103/PhysRevApplied.18.064071

I. INTRODUCTION

Recently, electron spin transport through a Si channel has generated considerable interest since the spin-orbit coupling (SOC) in bulk Si materials can yield electron transport with a long spin conservation length. This characteristic is attractive from the point of view of fundamental material physics and spin-functional device applications [1–9]. Based on the Elliott-Yafet (EY) mechanism that takes into account the Si band structure and acoustic phonon scattering [10,11], a spin flip occurs once in some electron momentum scattering events with a constant rate that is proportional to the strength of the SOC. Thus, when this mechanism is applicable, the ratio of electron momentum lifetime τ to the spin lifetime τ_S is constant, namely, the spin-flip probability (SFP) $\tau/\tau_S =$ constant. An additional spin scattering caused by the imperfection of the lattice, such as impurities and defects, was found to follow the EY mechanism [12]. This is regarded as an extrinsic property of Si. Experimental and theoretical studies on n-type bulk Si materials revealed that τ_S changes with dopant species and their volume concentrations. For instance, arsenic reduces τ_S by one order of magnitude more than phosphorous under a similar concentration [13,14]. On the other hand, a recent theory on optical phonon scattering predicts that the intervalley g and f processes are the spin-conserved and spin-flip scattering, respectively [15]. This is regarded as an intrinsic property of Si and has not yet been experimentally studied. Since it has been unclear whether the SFP differs depending on the electron momentum scattering process or not, it is necessary to clarify the SFP in a Si two-dimensional (2D) channel while the dominant electron momentum scattering process is changed.

To clarify electron spin transport in semiconductors, a very useful platform is a planar-type Si-based spin metal-oxide-semiconductor field-effect transistor (spin MOSFET) [16–18] with ferromagnetic source (S) and drain (D) electrodes and a $\mathrm{SiO_2/Si}$ gate stack. This is because electron spin transport through the Si 2D electron channel can be examined while the properties of the electron transport significantly change with the gate electric field E_G, lateral electric field E_L parallel to the electron transport, and temperature T.

---

[*] satodaikon@cryst.t.u-tokyo.ac.jp

[†] masaaki@ee.t.u-tokyo.ac.jp

[‡] nakane@cryst.t.u-tokyo.ac.jp

Using E_G and T, the electron distribution in the subbands in the Si 2D electron channel can be changed, which subsequently changes the dominant electron momentum scattering process during the transport. The background of this study and detailed electrical properties of the Si 2D channel are summarized in Supplemental Material [19]. These characteristics offer rich opportunities to systematically study the relation between electron momentum scattering and spin-flip scattering.

With decreasing T and fixing E_G in the middle range, the electron populations in the subbands with lower energies increase and the contribution of the phonon scattering to the electron momentum scattering is reduced. Using these features, the contribution of the phonon scattering to τ/τ_S can be estimated. Moreover, when a high electron mobility μ value, comparable to that in practical ordinary MOSFETs, is realized, τ/τ_S can be estimated when the dominant electron momentum scattering significantly changes in a wide E_G range. To date, τ/τ_S has never been estimated in the lower E_G range where the Coulomb scattering is dominant [8].

On the other hand, the spin conservation length λ_{eff} is also important for the establishment of spin-valve device guidelines. When we apply E_L, λ_{eff} changes while τ_S remains unchanged for a certain E_G and T. This phenomenon varies depending on the dominance of the spin diffusion or spin drift [20]: λ_{eff} approaches the spin diffusion length $\lambda_{\mathrm{diff}} = \sqrt{D_e\tau_S}$ near the diffusive transport limit with a low E_L, whereas λ_{eff} approaches the spin drift length $\lambda_{\mathrm{drift}} = \mu E_L \tau_S$ near the drift transport limit with a high E_L, where D_e and μ are the electron diffusion coefficient and electron mobility, respectively. The enhancement of λ_{eff} by the spin drift in a Si channel has been experimentally verified by other groups [6,21]. Our previous experiments on a Si-based spin MOSFET [8] demonstrated the spin drift effect at room temperature. We observed clear spin signals in a 10-μm-long 2D inversion channel under a high E_L although λ_{diff} at $E_L = 0$ V cm^{-1} was estimated to be approximately 1 μm. In consequence, the spin drift was found to be actually effective in the 2D inversion channel in the middle-to-higher E_G range. Since λ_{drift} is proportional to both μ and τ_S, an α times increase in τ under a constant τ/τ_S increases λ_{drift} by α^2 times. Therefore, it is expected that the enhancement of τ leads to the quadratic enhancement of spin conservation length.

In this paper, we study the electron spin transport in a Si 2D inversion channel with various μ values while E_G, T, and E_L are varied in a wide range to comprehensively understand the spin transport. The main purposes are as follows: (1) to deeply understand the spin transport in a Si channel by estimating τ/τ_S when the electronic properties and electron momentum scattering processes are changed, and (2) to estimate the increase in λ_{eff} when τ is increased. We measure both as-prepared and annealed spin MOSFET devices with low and high μ values, respectively, which enables us to quantitatively reveal changes in the spin transport with changes in the channel properties, by excluding device-to-device variability.

II. DEVICE STRUCTURE

Figure 1(a) shows a schematic of a back-gate-type spin MOSFET on a silicon-on-insulator (SOI) substrate with a 200-nm-thick SiO_2 buried oxide (BOX) layer used in this work. In this device, Fe/Mg/MgO/n^+-Si ferromagnetic tunnel junctions are used as the S and D, an 8-nm-thick p-Si channel with a boron doping concentration $N_A = 1 \times 10^{15}$ cm^{-3} has a length $L_{\mathrm{ch}} = 10$ μm and width $W_{\mathrm{ch}} = 180$ μm, the BOX layer is used as the gate dielectric, and reference electrodes L and R are located outside of the S and D, respectively. Note that the channel length L_{ch} is defined by the distance between the n^+-Si regions at the S and D. Figure 1(b) shows the detailed structure of the

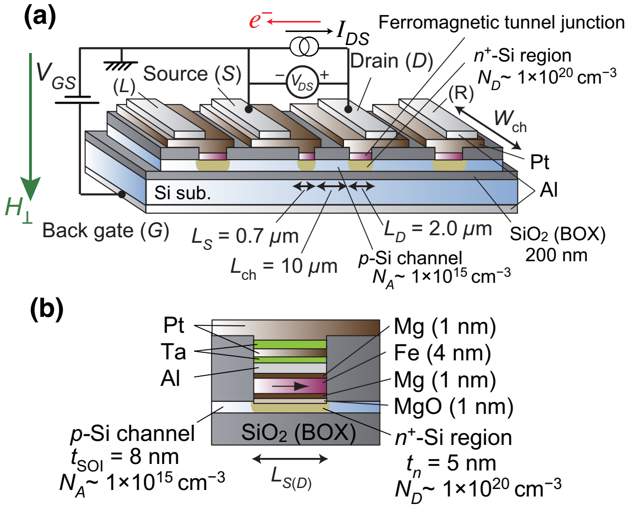

FIG. 1. (a) Schematic illustration of a spin metal-oxide-semiconductor field-effect transistor (spin MOSFET) examined in this work. This device is fabricated on a silicon-on-insulator substrate with a 200-nm-thick SiO_2 buried oxide (BOX) layer. All the top electrodes (S, D, L, and R) are Fe/Mg/MgO/n^+-Si ferromagnetic tunnel junctions with a lateral length $L_S = 0.7$ μm for the S and $L_D = 2.0$ μm for the D. An 8-nm-thick p-Si channel with a boron doping concentration $N_A = 1 \times 10^{15}$ cm^{-3} has a length $L_{\mathrm{ch}} = 10$ μm and a width $W_{\mathrm{ch}} = 180$ μm. The BOX layer is used as the gate dielectric, and reference electrodes L and R are located outside of the S and D, respectively. The measurement setup for two-terminal Hanle (2TH) signals is also illustrated: the voltage between the S and D is measured with a constant drain-to-source current I_{DS} and a constant gate-to-source voltage V_{GS} while an external perpendicular magnetic field $H_\perp$ is swept along the direction parallel to the green arrow. (b) Close up view of the Fe/Mg/MgO/n^+-Si ferromagnetic tunnel junctions at the top electrodes (S, D, L, and R), where the n^+-Si with a phosphorus doping concentration $N_D = 1 \times 10^{20}$ cm^{-3} has a thickness $t_n = 5$ nm.

ferromagnetic tunnel junctions at the S and D, in which the width of the bottom n^+-Si layer with a phosphorus doping concentration $N_D = 1.3 \times 10^{20}$ cm^{-3} is the same as the channel width ($W_{\rm ch} = 180$ μm), and $L_S = 0.7$ μm for the S and $L_D = 2.0$ μm for the D. On the same substrate, a back-gate-type Hall bar MOSFET with the same channel property and junction structure is also fabricated (see Supplemental Material [19]), where the channel length and width are 460 and 90 μm, respectively. The detailed fabrication process of the devices is described in Ref. [8]. We examine the electrical properties of the Si 2D inversion channel in two types of spin MOSFET devices (Fig. 1): (i) as-prepared device and (ii) annealed device. First, the as-prepared device is measured, annealed at 250 °C for 30 min in a N_2+ 4% H_2 ambient, and then the annealed device is measured. Both devices are measured under various bias and temperature conditions. The electron charge and spin transport are measured at $T = 4$, 77, 150, and 295 K to examine various scattering processes and electron distributions in the subbands. Note that the L and R electrodes are not used in this study.

III. ELECTRICAL PROPERTIES OF THE Si 2D INVERSION CHANNEL

Two methods are used to investigate the electrical properties of the Si 2D inversion channel: a Hall measurement with the Hall bar MOSFET and drain-to-source current I_{DS} *vs.* gate-to-source voltage V_{GS} measurement with the spin MOSFET. Then, the following parameters are estimated: μ, sheet electron density N_S, threshold gate voltage $V_{\rm th}$, and channel sheet resistance R_S. Next, the energy level and electron population at each subband are estimated using the experimental results and a self-consistent calculation using Schrödinger and Poisson equations [7,8,22]. Here, the effective electron conduction mass m^* is calculated by $m^* = \sum_i \sum_{\nu=2,4} m^{(\nu)} N_i^{(\nu)} / N_S$, where ν (=2 or 4) denotes the ν-fold subband group, $m^{(\nu)}$ denotes the effective mass in the ν-fold subband group ($m^{(2)} = 0.19$ and $m^{(4)} = 0.315$), i (=0, 1, 2, ...) denotes the subband number counted from the energy minimum of each subband group, and $N_i^{(\nu)}$ denotes the sheet electron density at the ith energy in the ν-fold subband group. Finally, τ values at various V_{GS} and T are estimated using the relation $\tau = m^* \mu / q$, where q is the elemental charge. To characterize the scattering process, μ and τ are plotted as a function of N_S.

Figures 2(a) and 2(b) show μ vs N_S, where open and closed circles are the estimated values of the as-prepared and annealed devices, respectively; different colors denote T; and dashed and solid lines connecting nearest-neighbor circles are guides. The μ-N_S curve for the as-prepared device [Fig. 2(a)] changes little with a decrease in T, which indicates that the temperature-insensitive Coulomb and surface roughness scattering processes govern the electron charge transport. In contrast, the μ-N_S curve of the annealed device [Fig. 2(b)] increases significantly with decreasing T, which indicates a decrease in the temperature-sensitive phonon scattering processes. In these figures, the scattering processes that determine the electron mobility are plotted using well-accepted formulae, where black solid, dotted, and bold lines denote Coulomb scattering ($\propto {N_S}^{+1}$), phonon scattering at 295 K ($\propto {N_S}^{-0.3}$), and surface roughness scattering ($\propto {N_S}^{-2}$), respectively [23]. Coulomb, phonon, and roughness scatterings are confirmed to be dominant in the lower, middle, and higher N_S ranges at 295 K, respectively, and Coulomb and roughness scatterings are dominant in the lower and higher N_S ranges at 4 K, respectively. The effect of the annealing on the μ-N_S curve shape can be clearly observed in the lower N_S range. With decreasing N_S, the μ curve for the as-prepared device bends towards the bottom at approximately 5×10^{12} cm^{-2}, whereas that for the annealed device bends at approximately 1.5×10^{12} cm^{-2}. Since Coulomb scattering is the dominant scattering process in the lower N_S range and it causes the μ-N_S curve to bend, the significant increase in μ after annealing is attributable to the reduction in the number of scattering events by Coulomb scattering, which is shown by the black solid lines in Figs. 2(a) and 2(b). It is most probable that hydrogen termination by annealing deactivates fixed charges either at the Si/SiO$_2$ interface or in the SiO$_2$ layer, leading to the reduction in the fixed defect state density [24]. This conclusion is supported by the experimental result where $V_{\rm th}$ is negatively shifted from 13 to 2 V due to annealing (see Supplemental Material [19]). It is noteworthy that the maximum $\mu = 3065$ cm^2 V^{-1} s^{-1} at 4 K is comparable to that (about 4000 cm^2 V^{-1} s^{-1}) at 25 K of a practical SOI MOSFET [25]. This clearly proves that our annealed device has a high-quality MOS gate stack with a low fixed defect state density.

Figures 2(c) and 2(d) show $N_i^{(\nu)}$ vs N_S plots calculated at 4 and 295 K, respectively, where red and pale red regions denote the electron populations at the twofold subband with the lowest ($i = 0$) and higher ($i = 1$–9) energy levels, respectively, and blue and pale blue regions denote the electron populations at the fourfold subband with the lowest ($i = 0$) and higher ($i = 1$–9) energy levels, respectively. The detailed calculation method is described in Supplemental Material of Refs. [7,8]. Here, we use $N_A = 10^{15}$ cm^{-3}, $t_{\rm Si} = 8$ nm, and other parameters taken from Ref. [22]. Below $N_S = 2 \times 10^{12}$ cm^{-2}, all the electrons are populated in the bottom energy level of the twofold subband at 4 K ($N_0^{(2)} = 100\%$), whereas electrons are distributed in various energy levels in the twofold and fourfold subband groups at 295 K. Figure 2(e) shows the $N_i^{(\nu)}$ *vs.* T plot calculated for $N_S = 2.3 \times 10^{12}$ cm^{-2}, where μ at 4 K for the annealed device shows the maximum value. Considering Figs. 2(a) and 2(b), the electron

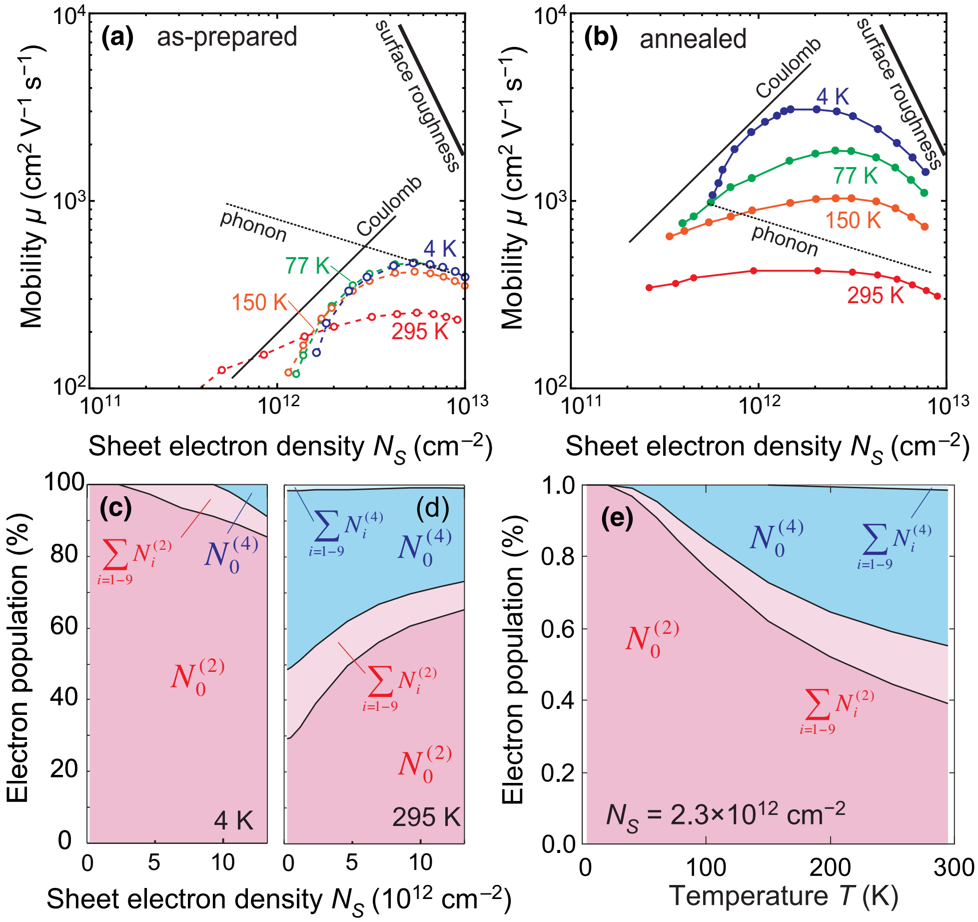

FIG. 2. (a),(b) Electron mobility μ versus sheet electron density N_S for the (a) as-prepared (open circles) and (b) annealed (closed circles) devices estimated from the electrical measurements at temperature T, where blue, green, orange, and red colors denote $T = 4$, 77, 150, and 295 K, respectively, and lines connecting nearest-neighbor circles are guides. The dominant scattering processes in μ are also estimated using the simple power law of N_S [23], where black solid, dotted, and bold lines denote the Coulomb ($\propto N_S{}^{+1}$), phonon ($\propto N_S{}^{-0.3}$), and surface roughness ($\propto N_S{}^{-2}$) scattering, respectively. (c)–(e) Electron population at each subband in the 2D Si channel at (c) 4 K and (d) 295 K vs N_S, and (e) at $N_S = 2.3 \times 10^{12}$ cm^{-2} vs T, which are obtained from the electrical properties estimated from the experiments and a self-consistent calculation with Schrödinger and Poisson equations (see Supplemental Material of Ref. [7]). We use $N_A = 10^{15}$ cm^{-3} and $t_{\mathrm{Si}} = 8$ nm, and other parameters are taken from Ref. [22]).

momentum scattering for the N_S value in Fig. 2(e) is as follows. In the as-prepared device, Coulomb scattering is dominant at all values of T. In the annealed device, Coulomb scattering is dominant at 4 K, intra- and intervalley phonon scattering processes contribute more with an increase in T, and finally the intra- and intervalley phonon scattering processes are dominant at 295 K. For detailed analysis of the temperature dependence, we calculate the phonon scattering rates at various temperatures using our self-consistent calculation (see Supplemental Material for the details [19]). We confirm that the contribution of the intervalley f process shows the largest increase among the phonon scattering processes with an increase in temperature; the contributions of the intervalley f and g processes steeply increase with an increase in temperature, and the former is more than 4 times greater than the latter above 200 K. Thus, we can mainly evaluate the contribution of the following scattering processes to the spin flip.

(1) Coulomb scattering

Since Coulomb scattering dominates at 4 K in both devices and annealing reduces the scattering rate, the contribution of Coulomb scattering can be evaluated by comparing the increase of τ and τ_S at 4 K.

(2) f-process intervalley phonon scattering

In the annealed device, the contribution of the intervalley f process increases the most with an increase in temperature. Therefore, the SFP due to the intervalley f process can be mainly evaluated when the temperature dependences of τ and τ_S are analyzed in the annealed device.

IV. ELECTRON SPIN TRANSPORT

To estimate τ_S in the Si 2D inversion channel, two-terminal Hanle spin precession signals (2TH signals) [26,27] are measured with the setup shown in Fig. 1(a). The voltage between the S and D is measured with a constant V_{GS} and I_{DS} (=5, 8, and 10 mA) while a perpendicular external magnetic field $H_\perp$ is applied and swept between ±3000 Oe. For measurements at various T, the V_{GS} value corresponding to the maximum μ at 295 K is used; at such V_{GS}, $N_S = 3.1 \times 10^{12}$ cm^{-2} for the as-prepared device and $N_S = 2.0 \times 10^{12}$ cm^{-2} for the annealed device. Under these N_S conditions, the electron distribution is calculated. Here, the result with $N_S = 2.3 \times 10^{12}$ cm^{-2} is shown in Fig. 2(e), since the electron distributions in these N_S values are almost identical with each other. In addition, 2TH signals are measured with various N_S, as shown in Table I.

Prior to the measurement of 2TH signals, the relative magnetization configuration of the S and D electrodes is set at the parallel (P) or antiparallel (AP) magnetization state using the major or minor loop of spin-valve signals with an in-plane external magnetic field. It is well known that voltage signals experimentally measured using the setup in Fig. 1(a) include both the spin transport and local spin accumulation signals [8,28–30]. In this study, we use the following formula to extract the spin transport signal, $\Delta V^{2\mathrm{TH}}(H_\perp) = [V^{\mathrm{AP}}(H_\perp) - V^{\mathrm{P}}(H_\perp)]/2$, where V^{AP} and V^{P} denote the voltage signals obtained in the AP and P magnetization states, respectively.

Figures 3(a) and 3(b) show 2TH signals at 4 K measured with $I_{DS} = 5$, 8, and 10 mA for the as-prepared and annealed devices, respectively, where red curves are experimental signals. In the 2TH signals, the oscillation and envelope originate from the in-phase and dephasing of the spin precession, respectively [1]. Hence, the clear Hanle precession curves in Figs. 3(a) and 3(b) represent the electron spin transport in both the as-prepared and annealed devices under all the bias conditions. In the same manner, 2TH signals are measured at various T. Figures 3(c) and 3(d) show Hanle precession signals measured at $T = 4$, 77, 150, and 295 K with $I_{DS} = 10$ mA for the as-prepared and annealed devices, respectively, where red curves are experimental signals. In both cases, the amplitude of the signal increases with a decrease in T, indicating that the spin polarization of electrons increases with decreasing T. When the signals at the same T of both devices are compared with each other, the number of the oscillation for the annealed device is larger than that for the as-prepared device. The increase in this number by the annealing indicates the suppression of spin dephasing, namely, the spin drift effect contributes more to the spin transport in the annealed device than in the as-prepared device. On the other hand, in each device, the magnetic field positions for the peak or valley in the oscillation remain unchanged when T is changed. It is clear that the drift velocity $v_d = \mu E_L$ remains constant with constant N_S and I_{DS} ($= qN_S v_d W_{\mathrm{ch}}$), although μ drastically changes ($\mu = 265$–441 cm^2 V^{-1} s^{-1} in the as-prepared device and $\mu = 451$–3065 cm^2 V^{-1} s^{-1} in the annealed device) when T is changed from 295 to 4 K.

TABLE I. N_S values used in the 2TH signal measurements for the as-prepared and annealed devices at various T.

	N_S (cm^{-2})			
T	4 K	77 K	150 K	295 K
As-prepared	3.1×10^{12}	3.1×10^{12}	3.1×10^{12}	3.1×10^{12}
	5.3×10^{12}			5.3×10^{12}
	7.6×10^{12}	7.6×10^{12}	7.6×10^{12}	7.6×10^{12}
Annealed	2.0×10^{12}	2.0×10^{12}	2.0×10^{12}	2.0×10^{12}
	4.3×10^{12}			4.3×10^{12}
	6.6×10^{12}	6.6×10^{12}	6.6×10^{12}	6.6×10^{12}

Next, all the 2TH signals are fitted using the following equation that takes into account the spin drift effect [8,20],

$$\Delta V^{\mathrm{2TH\text{-}P(AP)}}(H_\perp) = -\sigma^{\mathrm{P(AP)}} Re\left[\frac{{P_S}^2 I_{DS}}{X}\left(\frac{1}{r_{\mathrm{ch}}^{u}} + \frac{1}{r_{\mathrm{ch}}^{d}}\right)\exp\left(-\frac{L_{\mathrm{ch}}}{\hat{\lambda}_{\mathrm{ch}}^{d}}\right)\right], \tag{1}$$

$$X = \left(\frac{1}{r_{\mathrm{NL}}^{(S)}} + \frac{1}{r_{\mathrm{ch}}^{d}}\right)\left(\frac{1}{r_{\mathrm{NL}}^{(D)}} + \frac{1}{r_{\mathrm{ch}}^{u}}\right) - \left(\frac{1}{r_{\mathrm{NL}}^{(S)}} - \frac{1}{r_{\mathrm{ch}}^{u}}\right)\left(\frac{1}{r_{\mathrm{NL}}^{(D)}} - \frac{1}{r_{\mathrm{ch}}^{d}}\right)\exp\left(-\frac{L_{\mathrm{ch}}}{\hat{\lambda}_{\mathrm{ch}}^{u}} - \frac{L_{\mathrm{ch}}}{\hat{\lambda}_{\mathrm{ch}}^{d}}\right), \tag{2}$$

$$\frac{1}{\hat{\lambda}_{\mathrm{ch}}^{d(u)}} = -(+)\frac{\mu E_L}{2D_e} + \sqrt{\left(\frac{\mu E_L}{2D_e}\right)^2 + \left(\frac{1}{\hat{\lambda}_{\mathrm{ch}}}\right)^2}, \tag{3}$$

$$r_{\mathrm{NL}}^{S(D)} = \frac{r_{\mathrm{ch}} + r_n \tanh(L_{S(D)}/\hat{\lambda}_n)}{r_n + r_{\mathrm{ch}} \tanh(L_{S(D)}/\hat{\lambda}_n)} r_n, \tag{4}$$

where $\sigma^{\mathrm{P(AP)}} = +1(-1)$ is the sign factor for the P(AP) magnetization configuration, P_S is the tunneling spin polarization of the Fe/Mg/MgO/n^+-Si junction at the S and D electrodes, $r_{\mathrm{ch}} = R_S\hat{\lambda}_{\mathrm{ch}}/W_{\mathrm{ch}}$ is the intrinsic spin resistance in the inversion channel, $r_{\mathrm{ch}}^{u(d)} = R_S\hat{\lambda}_{\mathrm{ch}}^{d(u)}/W_{\mathrm{ch}}$ is the effective spin resistance with the spin drift in the inversion channel, $r_n = \rho_n\hat{\lambda}_n/t_n W_{\mathrm{ch}}$ is the spin resistance in the n^+-Si regions below the S and D electrodes, $L_S = 0.7$ μm and $L_D = 2.0$ μm are the n^+-Si region lengths parallel to the electron transport direction, $\hat{\lambda}_n = \sqrt{D_n\tau_n/(1 + i\gamma H_\perp \tau_n)}$ and $\hat{\lambda}_{\mathrm{ch}} = \sqrt{D_e\tau_S/(1 + i\gamma H_\perp \tau_S)}$ are the complex spin diffusion lengths [31] in the n^+-Si regions and inversion

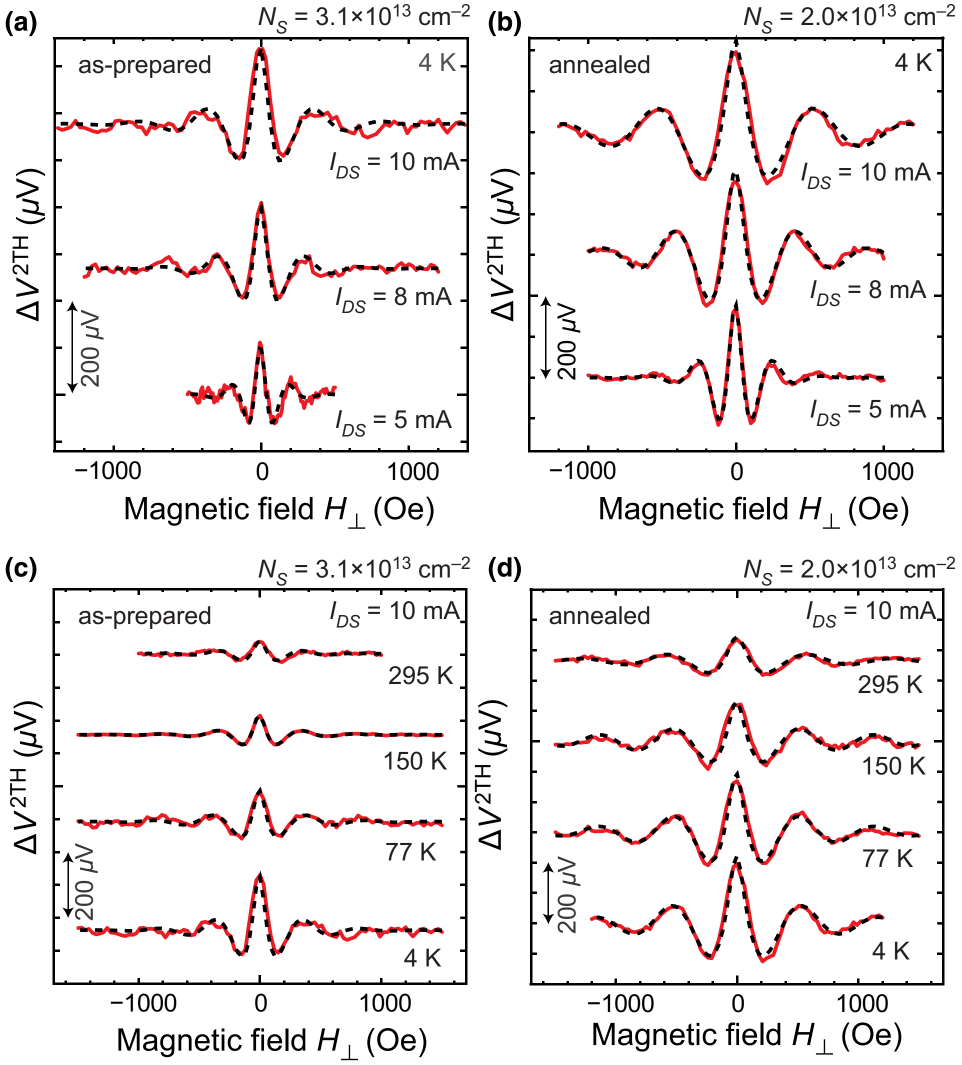

FIG. 3. (a),(b) Two-terminal Hanle signals ΔV^{2TH} measured at 4 K with $I_{DS} = 5$, 8, and 10 mA for the (a) as-prepared device and (b) annealed device, and (c),(d) ΔV^{2TH} measured at various temperatures ($T = 4$, 77, 150, and 295 K) with $I_{DS} = 10$ mA for the (c) as-prepared device and (d) annealed device, where N_S in (a),(c) and (b),(d) are 3.1×10^{12} and 2.0×10^{12} cm^{-2}, respectively. Red solid and black dashed curves represent the measured signals and fitting results, respectively. Each curve is vertically shifted for clear vision.

channel, respectively, and τ_n and D_n are the spin lifetime and electron diffusion coefficient in the n^+-Si regions, respectively. The effective spin resistance of the nonlocal regions $r_{\mathrm{NL}}^{S(D)}$ is the series spin resistance composed of r_n and r_{ch}. In the fitting, the experimentally estimated $\tau_n = 0.6$–0.8 ns and $D_n = 3.5$–4.4 cm^2 s^{-1} are used, as in our previous paper [8]. From Eq. (1), it is clear that the equation of $\Delta V^{\text{2TH-P(AP)}}$ is a nonlinear function of the various fitting parameters (P_S, τ_S, μ, and D_e). For highly accurate estimation, the signals with $I_{DS} = 5$, 8, and 10 mA are fitted so that all the fittings converge with the same D_e, μ, and τ_S that are independent of I_{DS}. As shown in Figs. 3(a)–3(d), the fitting curves (black dashed curves) almost perfectly reproduce all the experimental signals, from which we obtain $\tau_S = 1.4$ ns and $\mu = 410$ cm^2 V^{-1} s^{-1} for the as-prepared device and $\tau_S = 9.3$ ns and $\mu = 3074$ cm^2 V^{-1} s^{-1} for the annealed device. The validity of the fittings is supported by the fact that the μ values estimated from the 2TH signals are almost identical with those estimated from the electrical measurements, as shown in Figs. 4(a) and 4(b). In the same manner, the 2TH signals measured at various temperatures are fitted by Eq. (1), as shown by black dashed curves in Figs. 3(c) and 3(d). As in the case of 4 K, the experimental and fitting curves agree very well with each other.

V. SPIN-FLIP PROBABILITY AND THE SPIN CONSERVATION LENGTH

Figures 5(a) and 5(b) show τ_S and τ plotted as a function of N_S for the as-prepared and annealed devices, respectively, and Fig. 5(c) shows τ_S and τ plotted as a function of T, where squares are τ_S estimated from the 2TH signals, circles are τ estimated from the electrical measurements [Figs. 2(a) and 2(b)], and left and right vertical axes represent the scales for τ_S and τ, respectively. Note that the scale of the left axis is 25 000 times larger than that of the right axis in Figs. 5(a)–5(c). As described in Sec. III, we discuss the contributions of the (1) Coulomb scattering and

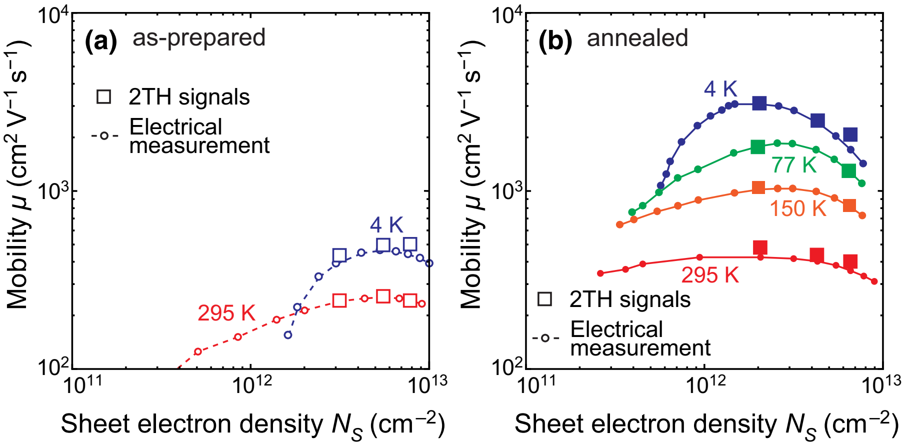

FIG. 4. (a),(b) Electron mobility μ versus sheet electron density N_S, which are estimated for the (a) as-prepared device and (b) annealed device. (a) Open squares are the μ values estimated from the 2TH signals and open circles with a dashed line are the μ values estimated from the electrical measurements [Fig. 2(a)]. Blue and red colors denote $T = 4$ and 295 K, respectively. (b) Closed squares are the μ values estimated from the 2TH signals, and closed circles with a solid line are the μ values estimated from the electrical measurements [Fig. 2(b)]. Blue, green, orange, and red colors denote $T = 4$, 77, 150, and 295 K, respectively.

(2) *f-process intervalley* phonon scattering to the spin flip based on our experimental results and theoretical fittings.

(1) Coulomb scattering

As shown by the blue symbols in Figs. 5(a) and 5(b), both τ_S and τ at 4 K are increased approximately 6 times by the H_2 annealing while the ratio τ/τ_S ($\sim$1/25 000) remains unchanged, indicating that the SFP of Coulomb scattering is approximately 1/25 000.

(2) *f*-process intervalley phonon scattering

As shown by the filled symbols in Fig. 5(c), τ_S and τ in the annealed device have almost the same temperature dependences, indicating that the SFP of f-process intervalley scattering is approximately 1/25 000.

From the these results, we find τ/τ_S is almost constant at approximately 1/25 000 under any conditions, i.e., the EY mechanism dominates the SFP ($= \tau/\tau_S$) in the Si 2D inversion channel even when the electrical properties and dominant scattering process change significantly. The EY mechanism is supported by the increased τ_S with increase in μ by the reduction in the fixed defect state density due to annealing. This is because the anticorrelation between τ_S and μ should be obtained when the D'yakonov-Perel' (DP) process is dominant [32,33]. It should be noted that the τ/τ_S value (approximately 1/25 000) in the p-Si channel with light boron doping ($N_A = 1 \times 10^{15}$ cm^{-3}) is smaller than that (around 1/14 000) in the phosphorous-doped 2D accumulation channel ($N_D = 1 \times 10^{17}$ cm^{-3}) when $T = 295$ K [8]. Considering that ionized dopant atoms can also be spin-flip scattering centers at 295 K, they likely originate from the differences in the channel properties, such as the doping concentration and dopant atoms.

From Ref. [20], λ_{eff} is given by

$$\lambda_{\text{eff}} = \left[-\frac{\mu E_L}{2D_e} + \sqrt{\left(\frac{\mu E_L}{2D_e}\right)^2 + \left(\frac{1}{\lambda_{\text{diff}}}\right)^2} \right]^{-1}$$

$$= \frac{\lambda_{\text{drift}} + \sqrt{\lambda_{\text{drift}}{}^2 + 4\lambda_{\text{diff}}{}^2}}{2}, \qquad (5)$$

where $\lambda_{\text{diff}} = \sqrt{D_e \tau_S}$ and $\lambda_{\text{drift}} = \mu E_L \tau_S$. To further understand the spin-transport physics, it is worth plotting the values of λ_{eff} estimated from Eq. (5) for a wide range of E_L [Fig. 5(d)]. The open and closed circles are the values obtained from Eq. (5) for the electric fields used in the experiments for the as-prepared and annealed devices, respectively, with the values of τ_S, μ, and D_e as input. The dashed and solid lines are obtained from Eq. (5) for other values of the electric field for the as-prepared and annealed devices, respectively. When E_L increases, the dashed curves for the as-prepared device show a gradual increase at first, followed by a drastic increase. The former and latter increases correspond to the diffusion-dominated λ_{eff} ($\sim\lambda_{\text{diff}}$) and drift-dominated λ_{eff} ($\sim\lambda_{\text{drift}}$), respectively. Regarding the solid curves for the annealed device, the λ_{eff}-E_L curves at 4 and 77 K show a monotonic increase due to the drift-dominated λ_{eff} in the entire E_L range, which is confirmed by the fact that these lines are parallel to the drift-dominated λ_{eff} for the as-prepared device. From these features, it can be concluded that all the experimental results denoted by the closed and open circles are λ_{eff} enhanced by the spin drift.

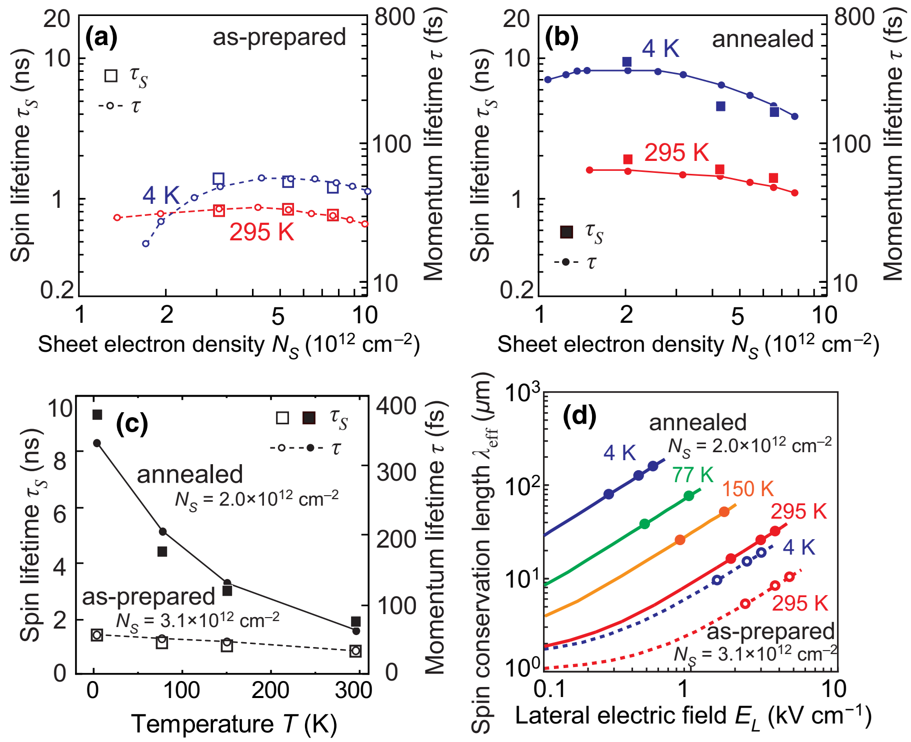

FIG. 5. (a),(b) Spin lifetime τ_S and electron momentum lifetime τ plotted as a function of the sheet electron density N_S, which are estimated for the (a) as-prepared device and (b) annealed device. Left and right vertical axes represent the scales for τ_S and τ, respectively. (a) Open squares are the τ_S values estimated from the 2TH signals and open circles with a dashed line are the τ values estimated from the electrical measurements [Fig. 2(a)]. Blue and red colors denote $T = 4$ and 295 K, respectively. (b) Closed squares are the τ_S values estimated from the 2TH signals, and closed circles with a solid line are the τ values estimated from the electrical measurements [Fig. 2(b)]. Blue and red colors denote $T = 4$ and 295 K, respectively. (c) τ_S and τ plotted as a function of T, where open circles/squares and closed circles/squares are estimated values for the as-prepared ($N_S = 3.1 \times 10^{12}$) and annealed devices ($N_S = 2.0 \times 10^{12}$), respectively. Left and right vertical axes represent the scales for τ_S and τ, respectively. Squares are the τ_S values estimated from the 2TH signals and circles with a dashed or solid line are the τ values estimated from the electrical measurements [Figs. 2(a) and 2(b)]. (d) Spin conservation length λ_{eff} obtained using Eq. (5) and the experimentally determined parameters τ_S, μ, and D_e, plotted as a function of E_L. Open and closed circles are the values obtained using Eq. (5) for E_L used in the experiments for the as-prepared and annealed devices, respectively. The dashed and solid lines are those obtained using Eq. (5) for other values of E_L for the as-prepared and annealed devices, respectively. Blue, green, orange, and red colors denote $T = 4$, 77, 150, and 295 K, respectively.

For a deeper understanding of electron spin transport in the Si 2D inversion channel, it is also important to analyze λ_{eff} and the spin conservation efficiency η_{S} during the transport through the 10-μm-long inversion channel. Based on the spin drift-diffusion model, λ_{eff} values for the as-prepared and annealed devices are estimated to be 3.9 and 159 μm, respectively, as shown in Fig. 5(d), where $E_L = 556$ Vcm^{-1} at 4 K corresponds to $I_{DS} = 10$ mA in the annealed device. Using these values and $\eta_{\mathrm{S}} = \exp(-L_{\mathrm{ch}}/\lambda_{\mathrm{eff}})$ with $L_{\mathrm{ch}} = 10$ μm, we obtain $\eta_{\mathrm{S}} = 8\%$ in the as-prepared device and $\eta_{\mathrm{S}} = 94\%$ in the annealed device, indicating that η_{S} is dramatically enhanced by the annealing. Note that, in our spin MOSFET structure, the signal amplitude is mostly determined by the spin resistance of the n^+-Si region at the D junction (see discussion in Ref. [8]). Since the properties of the n^+-Si region remain unchanged by the annealing at 250 °C, the absolute amplitudes of the Hanle signals in Figs. 3(b) and 3(d) are not greatly increased. Combining the enhancement of the spin transport efficiency developed in this study with the appropriate device structure proposed in our previous paper [8], significant improvement in the spin transport signal as well as transistor characteristics is expected.

VI. DISCUSSION

Our experiments and analyses reveal that the spin MOSFETs with high and low μ values have constant SFP $= \tau/\tau_S \sim 1/25\,000$ under any bias current and T conditions, namely, the SFP is determined by the EY mechanism even when the channel properties are greatly changed.

So far, the changes in τ_S in a Si 2D channel with temperature have not been clarified, to the best of our knowledge. Thus, it is worth noting that the change in τ_S in Fig. 5(c) is less than 10 times in the T range 4–295 K, which is more gradual than that of a theoretical model and experimental results in bulk Si. When only the phonon scattering in Si bulk materials is considered, theory predicts that the τ_S-T relation follows a $T^{-5/2}$ law [11], whereas electron spin resonance and spin transport experiments reveal that the τ_S-T relation follows a T^{-3} law [30]. This is likely to be because, in Si 2D channels, Coulomb scattering is dominant at low temperatures, that is, it limits τ where the strength of phonon scattering is weak (see Sec. S1 in Supplemental Material [19]). On the other hand, at 295 K, $\tau_S = 1.9$ ns for the annealed device, as shown in Fig. 5(c), which is significantly smaller than $\tau_S \sim 8$ ns in the experimental results of Si bulk materials [34]. This is probably due to the quantum confinement of the channel. In Si 2D channels, the strength of phonon scattering is enhanced by a form factor, determined by envelope wave functions of both the initial and final states in the scattering process [25,35]. Our self-consistent calculation reveals that the phonon scattering strength is enhanced by approximately 3 times in our device with an 8-nm-thick channel [19], which reasonably explains $\tau_S = 1.9$ ns for the annealed device. This consideration cannot be applied to the as-prepared device because Coulomb scattering is dominant at any temperature, as shown in Fig. 5(c).

The detailed τ/τ_S values at different temperatures may explain the physics of the electron spin transport. In the plot for the annealed device in Fig. 5(c), there are differences between the open and closed circles, particularly at 4 and 77 K. The τ/τ_S value at 4 K is larger by 16% than 1/25 000, whereas that at 77 K is smaller by 11% than 1/25 000. We consider that the deviation indicates the difference in the SFP between the dominant scattering processes. Nevertheless, the SFP remains nearly unchanged depending on the momentum scattering process.

Here, we would like to briefly overview the SFP values reported in other materials where the EY mechanism through phonon scattering processes is dominant. As summarized in Ref. [36], the SFP in Al and Cu are estimated to be approximately 1/10 000 and 1/1000, respectively, by several experiments on bulk materials, films, and nanowires, as well as theoretical studies. On the other hand, the SFP in an 85-nm-thick n^+-Si with a phosphorus doping concentration of approximately 5×10^{19} cm^{-3} was estimated to be approximately 1/100 000 by a spin transport experiment [37]. From the general knowledge that larger atomic number Z leads to larger SOC [38], the order of the SFP values in Al, Cu, and the Si 2D channel can be simply understood: Al ($Z = 13$), Cu ($Z = 29$), and Si ($Z = 14$). Despite the single-crystalline Si with the same dopant atoms in both cases, the SFP value in the Si 2D channel is 4 times that in the n^+-Si channel. To the best of our knowledge, although the reason for the difference is yet unclear, SOC in the 2D channel can become larger than that in Si bulk materials. A possible origin for the increase of SOC is the spatial symmetry breaking along the vertical direction in the 2D channel, as suggested in our previous paper [8].

Next, we focus on the electron spin scattering in the annealed device at 4 K, where Coulomb scattering is dominant, all the electrons are populated at the bottom energy level of the twofold subband, the dopant boron accepter atoms are frozen out, and the fixed defect states are localized at the Si/SiO$_2$ interface and in the SiO$_2$ layer. Under such circumstances, the electron momentum scattering occurs through the intravalley scattering owing to the fixed defect states in the SiO$_2$ layer [39,40]. On the other hand, although a theory on the impurity-dominated electron spin-flip scattering in Si 2D inversion channels has been reported [32], it cannot be applied to our analysis because it assumes that dopant atoms are ionized and the electron spin flip occurs through the intervalley f process between the twofold and fourfold subbands even at low temperatures. Besides, as pointed out in Ref. [32], the spin flip due to the Coulomb scattering through fixed defect states near a SiO$_2$/Si interface has not been clarified. To qualitatively analyze the effect of Coulomb scattering, the strength of the SOC is estimated using the theory in Ref. [12]. From the difference in V_{th} between the theoretical and experimental values in the annealed device, the fixed defect states density N_{def} is estimated to be 2.3×10^{11} cm^{-2} [19], which corresponds to the volume density $n_{\text{def}} = 1 \times 10^{17}$ cm^{-3}, according to the conversion procedure from the sheet to volume densities in Ref. [32]. Using this n_{def} value and $\tau_S = 9.3$ ns, the theory in Ref. [12] predicts that the fixed defect states in SiO$_2$ have an SOC effectively 2.3 times larger than that for Sb dopant atoms. Thus, further theoretical consideration is needed to completely clarify the spin-flip scattering due to the Coulomb scattering caused by defects. We speculate that spin at Si^{3+} in our SiO$_2$ layer and screening potentials for ionized defects may have an influence on the electron spin scattering [12,41].

Our finding leads to a simple guideline that τ_S at room temperature is enhanced by the enhancement of μ. This conclusion is also supported by our result that even the highest μ value of 3065 cm^2 V^{-1} s^{-1} at 4 K is not high enough for the appearance of the DP mechanism [32]. Hence, it is important to note that the established Si technology for the enhancement of μ in ordinary MOSFETs is also useful for spin MOSFETs, as we demonstrate that the SiO$_2$/Si interface with the lower N_{def} achieved by annealing leads to the higher τ_S value at a certain T than that with the higher N_{def}. In Fig. 2(b), although the higher μ values are realized by annealing, they are slightly lower than the universal mobility of ordinary MOSFETs with a bulk Si substrate. Since this arises from the enhancement of phonon scattering due to the channel confinement [25], higher τ_S can be obtained using a thicker SOI channel layer or a top-gated spin MOSFET with a bulk Si substrate. On the other hand, since τ_S increases with a decrease in temperature in the annealed device, as shown in Fig. 5(c), the suppression of the intervalley scattering effectively increases τ_S through the increase in the population at the lowest-energy twofold subband, as theoretically predicted in Ref. [32].

At present, the factor governing the τ/τ_S value is still an open question; in particular, there is still a lack of theory on spin-flip scattering due to Coulomb scattering. Therefore, further experimental and theoretical studies are needed to accumulate the knowledge on the physics of electron spin transport in Si 2D inversion channels.

VII. SUMMARY

We study the electron charge and spin transport properties in 10-μm-long Si 2D inversion channels using the spin MOSFET with the low and high electron mobility μ values. The electron momentum lifetime τ and spin lifetime τ_S are estimated from the electrical characteristics and 2T Hanle precession signals, respectively, under various bias and temperature ($T = 4$, 77, 150, and 295 K) conditions. The spin-flip probability τ/τ_S for different μ values is found to be approximately 1/25 000 under any bias and temperature conditions, indicating that it is governed by the EY mechanism even when the dominant electron momentum scattering process is greatly changed. Owing to the almost constant τ/τ_S, the estimated spin conservation length λ_{eff} increases with increasing μ, caused by the combination of the spin drift and EY mechanism.

In the spin MOSFET with the high μ value, the nearly ideal spin conservation efficiency 94% is achieved at 4 K where the intravalley scattering due to Coulomb scattering is dominant. This result indicates that the suppression of the intervalley scattering is the key to higher τ_S and λ_{eff}. Our systematic and quantitative results including the experiments and theory contribute to advances in both the physics and device applications of spin transport in a Si 2D channel.

ACKNOWLEDGMENTS

This work was supported in part by Grants-in-Aid for Scientific Research (Grants No. 18H05345, No. 20H05650), CREST of JST (Grant No. JPMJCR1777), and Spintronics Research Network of Japan.

[1] B. Huang, D. J. Monsma, and I. Appelbaum, Coherent Spin Transport through a 350 Micron Thick Silicon Wafer, Phys. Rev. Lett. **99**, 177209 (2007).

[2] O. M. J. van ‘t Erve, A. T. Hanbicki, M. Holub, C. H. Li, C. Awo-Affouda, P. E. Thompson, and B. T. Jonker, Electrical injection and detection of spin-polarized carriers in silicon in a lateral transport geometry, Appl. Phys. Lett. **91**, 212109 (2007).

[3] H.-J. Jang and I. Appelbaum, Spin Polarized Electron Transport near the Si/SiO^2 Interface, Phys. Rev. Lett. **103**, 117202 (2009).

[4] T. Suzuki, T. Sasaki, T. Oikawa, M. Shiraishi, Y. Suzuki, and K. Noguchi, Room-temperature electron spin transport in a highly doped Si channel, Appl. Phys. Express **4**, 023003 (2011).

[5] R. Nakane, T. Harada, K. Sugiura, and M. Tanaka, Magnetoresistance of a spin metal–oxide–semiconductor field-effect transistor with ferromagnetic MnAs source and drain contacts, Jpn. J. Appl. Phys. **49**, 113001 (2010).

[6] T. Sasaki, Y. Ando, M. Kameno, T. Tahara, H. Koike, T. Oikawa, T. Suzuki, and M. Shiraishi, Spin Transport in Nondegenerate Si with a Spin MOSFET Structure at Room Temperature, Phys. Rev. Appl. **2**, 034005 (2014).

[7] S. Sato, M. Ichihara, M. Tanaka, and R. Nakane, Electron spin and momentum lifetimes in two-dimensional Si accumulation channels: Demonstration of Schottky-Barrier spin metal-oxide-semiconductor field-effect transistors at room temperature, Phys. Rev. B **99**, 165301 (2019).

[8] S. Sato, M. Tanaka, and R. Nakane, Spin transport in Si-based spin metal-oxide-semiconductor field-effect transistors: Spin drift effect in the inversion channel and spin relaxation in the n^+-Si source/drain regions, Phys. Rev. B **102**, 035305 (2020).

[9] R. Nakane, S. Sato, and M. Tanaka, Enhancement of room-temperature effective spin diffusion length in a Si-based spin MOSFET with an inversion channel, IEEE J. Electron Devices Soc. **8**, 807 (2020).

[10] R. J. Elliott, Theory of the effect of spin-orbit coupling on magnetic resonance in some semiconductors, Phys. Rev. **96**, 266 (1954).

[11] Y. Yafet, in *Solid State Physics*, edited by F. Seitz and D. Turnbull (Academic Press, New York, 1963), Vol. 14.

[12] Y. Song, O. Chalaev, and H. Dery, Donor-Driven Spin Relaxation in Multivalley Semiconductors, Phys. Rev. Lett. **113**, 167201 (2014).

[13] J. H. Pifer, Microwave conductivity and conduction-electron spin-resonance linewidth of heavily doped Si: P and Si: As, Phys. Rev. B **12**, 4391 (1975).

[14] R. Jansen, S. P. Dash, S. Sharma, and B. C. Min, Semicond, silicon spintronics with ferromagnetic tunnel devices, Sci. Technol. **27**, 083001 (2012).

[15] Y. Song and H. Dery, Analysis of phonon-induced spin relaxation processes in silicon, Phys. Rev. B **86**, 085201 (2012).

[16] S. Sugahara and M. Tanaka, A spin metal–oxide–semiconductor field-effect transistor using half-metallic-ferromagnet contacts for the source and drain, Appl. Phys. Lett. **84**, 13 (2004).

[17] S. Sugahara and M. Tanaka, Spin MOSFETs as a basis for spintronics, ACM Trans. Storage **2**, 197 (2006).

[18] M. Tanaka and S. Sugahara, A spin metal-oxide-semiconductor field-effect transistor (spin MOSFET) with a ferromagnetic semiconductor for the channel, IEEE Trans. Electron Devices **54**, 961 (2007).

[19] See Supplemental Material at http://link.aps.org/supplemental/10.1103/PhysRevApplied.18.064071 for (S1) Electrical properties of the 2D Si channel and (S2) Hallbar device and the Hall measurement.

[20] Z. G. Yu and M. E. Flatte, Spin diffusion and injection in semiconductor structures: Electric field effects, Phys. Rev. B **66**, 235302 (2002).

[21] A. Spiesser, Y. Fujita, H. Saito, S. Yamada, K. Hamaya, W. Mizubayashi, K. Endo, S. Yuasa, and R. Jansen, Quantification of Spin Drift in Devices with a Heavily Doped Si Channel, Phys. Rev. Appl. **11**, 044020 (2019).

[22] S. Takagi, J. L. Hoyt, J. J. Weiser, and J. F. Gibbons, Comparative study of phonon-limited mobility of two-dimensional electrons in strained and unstrained Si metal–oxide–semiconductor field-effect transistors, J. Appl. Phys. **80**, 1567 (1996).

[23] S. Takagi, A. Toriumi, M. Iwase, and H. Tango, On the universality of inversion layer mobility in Si MOSFET's: Part I-effects of substrate impurity concentration, IEEE Trans. Electron Devices **41**, 2363 (1994).

[24] E. H. Nicollian and J. R. Brews, *MOS (Metal Oxide Semiconductor) Physics and Technology* (Wiley, New York, 1982), Chapter 15.

[25] K. Uchida, J. Koga, and S. Takagi, Experimental study on electron mobility in ultrathin-body silicon-on-insulator metal-oxide-semiconductor field-effect transistors, J. Appl. Phys. **102**, 074510 (2007).

[26] F. J. Jedema, H. B. Heersche, A. T. Filip, J. J. A. Baselmans, and B. J. van Wees, Electrical detection of spin precession in a metallic mesoscopic spin valve, Nature **416**, 713 (2002).

[27] F. J. Jedema, M. V. Costache, H. B. Heersche, J. J. A. Baselmans, and B. J. van Wees, Electrical detection of spin accumulation and spin precession at room temperature in metallic spin valves, Appl. Phys. Lett. **81**, 5162 (2002).

[28] X. Lou, C. Adelmann, M. Furis, S. A. Crooker, C. J. Palmstrøm, and P. A. Crowell, Electrical Detection of Spin Accumulation at a Ferromagnet-Semiconductor Interface, Phys. Rev. Lett. **96**, 176603 (2006).

[29] A. Spiesser, Y. Fujita, H. Saito, S. Yamada, K. Hamaya, S. Yuasa, and R. Jansen, Hanle spin precession in a two-terminal lateral spin valve, Appl. Phys. Lett. **114**, 242401 (2019).

[30] R. Jansen, A. Spiesser, Y. Fujita, H. Saito, S. Yamada, K. Hamaya, and S. Yuasa, Superimposed contributions to two-terminal and nonlocal spin signals in lateral spin-transport devices, Phys. Rev. B **104**, 144419 (2021).

[31] S. Sato, R. Nakane, T. Hada, and M. Tanaka, Spin injection into silicon in three-terminal vertical and four-terminal lateral devices with Fe/Mg/MgO/Si tunnel junctions having an ultrathin Mg insertion layer, Phys. Rev. B **96**, 235204 (2017).

[32] Y. Song and D. Sarma, Impurity-Driven Two-Dimensional Spin Relaxation Induced by Intervalley Spin-Flip Scattering in Silicon, Phys. Rev. Appl. **7**, 014003 (2017).

[33] P. Boross, B. Dóra, A. Kiss, and F. Simon, A unified theory of spin-relaxation due to spin-orbit coupling in metals and semiconductors, Sci. Rep. **3**, 3233 (2013).

[34] J. L. Cheng, M. W. Wu, and J. Fabian, Theory of the Spin Relaxation of Conduction Electrons in Silicon, Phys. Rev. Lett. **104**, 016601 (2010).

[35] M. Lundstrom, *Fundamentals of Carrier Transport* (Cambridge University Press, Cambridge, UK, 2000), Chapter 2.

[36] F. J. Jedema, M. S. Nijboer, A. T. Filip, and B. J. van Wees, Spin injection and spin accumulation in all-metal mesoscopic spin valves, Phys. Rev. B **67**, 085319 (2003).

[37] S. Lee, N. Yamashita, Y. Ando, S. Miwa, Y. Suzuki, H. Koike, and M. Shiraishi, Investigation of spin scattering mechanism in silicon channels of Fe/MgO/Si lateral spin valves, Appl. Phys. Lett. **110**, 192401 (2017).

[38] K. V. Shanavas, Z. S. Popović, and S. Satpathy, Theoretical model for Rashba spin-orbit interaction in *d* electrons, Phys. Rev. B **90**, 165108 (2014).

[39] David Esseni, Pierpaolo Palestri, and Luca Selmi, *Nanoscale MOS Transistors: Semi-Classical Transport and Applications* (Cambridge University Press, Cambridge, UK, 2011), Chapter 4.

[40] N. D. Arora and G. Sh. Gildenblat, A semi-empirical model of the MOSFET inversion layer mobility for low-temperature operation, IEEE Trans. Electron Devices **34**, 89 (1987).

[41] Y. Nishi, Study of silicon-silicon dioxide structure by electron spin resonance I, Jpn. J. Appl. Phys. **10**, 52 (1971).